PHYSICAL REVIEW B **101**, 195122 (2020)

Magnetic phase diagram and magnetoelastic coupling of $NiTiO_3$

K. Dey,[1,*,†] S. Sauerland,[1,†] J. Werner,[1] Y. Skourski,[2] M. Abdel-Hafiez,[3] R. Bag,[4] S. Singh,[4] and R. Klingeler[1,5]
[1]*Kirchhoff Institute of Physics, Heidelberg University, INF 227, D-69120 Heidelberg, Germany*
[2]*Dresden High Magnetic Field Laboratory (HLD-EMFL), Helmholtz-Zentrum Dresden Rossendorf, D-01314 Dresden, Germany*
[3]*Harvard University, Cambridge, Massachusetts 02138, USA*
[4]*Indian Institute of Science Education and Research, Pune, Maharashtra 411008, India*
[5]*Centre for Advanced Materials (CAM), Heidelberg University, INF 225, D-69120 Heidelberg, Germany*

(Received 14 February 2020; revised manuscript received 31 March 2020; accepted 23 April 2020; published 13 May 2020)

We report high-resolution dilatometry on high-quality single crystals of $NiTiO_3$ grown by means of the optical floating-zone technique. The anisotropic magnetic phase diagram is constructed from thermal expansion and magnetostriction studies up to $B = 15$ T and magnetization studies in static (15-T) and pulsed (60-T) magnetic fields. Our data allow us to quantitatively study magnetoelastic coupling and to determine uniaxial pressure dependencies. While the entropy changes are found to be of magnetic nature, Grüneisen analysis implies only one relevant energy scale in the whole low-temperature regime. Thereby, our data suggest that the observed structural changes due to magnetoelastic coupling and previously reported magnetodielectric coupling [L. Balhorn, J. Hazi, M. C. Kemei, and R. Seshadri, Phys. Rev. B **93**, 104404 (2016)] are driven by the same *magnetic* degrees of freedom that lead to long-range magnetic order in $NiTiO_3$.

DOI: 10.1103/PhysRevB.101.195122

I. INTRODUCTION

The search for new multiferroics, i.e., materials concomitantly exhibiting various ferroic orders such as magnetic and electric order coupled to each other [1], has revived interest in the family of ilmenite-structured compounds. There are various titanates $M\mathrm{TiO}_3$ (M = Mn, Fe, Co, Ni) which crystallize in the ilmenite structure within the space group R-3. The crystal structure consists of alternate layers of corner sharing TiO_6 and MO_6 octahedra stacked along the c axis [2]. Previous magnetic [3–5] and powder neutron diffraction studies [6–9] report that long-range antiferromagnetic (AFM) order evolving at low temperatures is of the G type for $MnTiO_3$, and of the A type for $FeTiO_3$, $CoTiO_3$, and $NiTiO_3$. In the ordered phase, the magnetic moments associated with M^{2+} ions are collinearly arranged along the c axis in $MnTiO_3$ and with a slight spin tilting of 1.6° away from the c axis in $FeTiO_3$. The easy-plane-type AFM order in $CoTiO_3$ and $NiTiO_3$ is characterised by spins lying in the ferromagnetic ab layers which are aligned antiferromagnetically along c. In $FeTiO_3$, the onset of long-range magnetic order, at T_N, is associated with significant changes of the lattice parameters indicating magnetoelastic coupling [9]. Magnetodielectric and polarization measurements on $MnTiO_3$ show an anomaly in the dielectric permittivity, ϵ, at T_N, while finite polarization is found in applied external magnetic fields indicating that it may realize a linear magnetoelectric material [10]. Both in $CoTiO_3$ and $NiTiO_3$, anomalies in ϵ at T_N and a strong field dependent magnetocapacitance in the ordered state indicate the presence of large magnetodielectric coupling [11]. Furthermore, the observation of Dirac magnons in $CoTiO_3$ from recent inelastic neutron scattering studies [12] has peaked interest in this series of materials. Despite clear evidence of pronounced magnetodielectric coupling in all known $M\mathrm{TiO}_3$, its origin and mechanism have not yet been elucidated. In order to address this question, we have grown large, high-quality single crystals of $NiTiO_3$ by means of the optical floating-zone technique under various atmospheres and at different pressure. The single crystals were used for high-resolution studies of thermal expansion and magnetostriction along the crystallographic a and c axes, respectively. Though such investigations have been shown to provide detailed insight into underlying mechanism of multiferroics (see, e.g., Refs. [13–18], there are no high-resolution dilatometry studies on $M\mathrm{TiO}_3$ single crystals yet. In addition, comparing the magnetic length and entropy changes as detected by thermal expansion coefficients and specific heat allow determining the uniaxial and hydrostatic pressure dependencies by means of Grüneisen scaling. Analysis of the Grüneisen ratio, i.e., the ratio of thermal expansion coefficient and heat capacity, has been particularly suggested by Spaldin *et al.* for the related compound $EuTiO_3$ as it can clarify the potential multiferroic quantum critical nature [19]. Our dilatometry studies are accompanied by magnetization studies in static (15-T) and pulsed (60-T) magnetic fields which enable constructing the anisotropic phase diagram in $NiTiO_3$ which has not been established yet.

II. EXPERIMENTAL METHODS

$NiTiO_3$ powder was prepared via standard solid-state reaction of stoichiometric amounts of NiO and TiO_2 between

---

[*] kaustav.dey@kip.uni-heidelberg.de

[†] These authors contributed equally to this work.

1150° and 1350 °C with several intermediate grinding steps. The powder was made into rods of length 10 cm and 5 mm in diameter by hydrostatically pressing the powders at 700 bar and annealing them for 24 h at 1350 °C. Single crystals of $NiTiO_3$ were grown in a four-mirror optical floating-zone furnace (Crystal system corporation, Japan) equipped with 4×150 W halogen lamps at IISER Pune and in a two mirror high-pressure optical floating-zone furnace (HKZ, SciDre) equipped with a 3500-W Xe arc lamp at Heidelberg University. Macroscopic single crystals were grown at 3 mm/h under various atmospheres and up to 5 bar pressure. Phase purity of the powder and the ground single crystals was studied by means of powder x-ray diffraction measurements on a Bruker D8 Advance ECO diffractometer with Cu-Kα source. Laue diffraction in back scattering geometry was performed to study the crystallinity and to orient the single crystals. Structural Rietveld refinements were carried out using the Full Prof suite 2.0 [20].

Static magnetization $\chi = M/B$ was studied in magnetic fields up to 15 T applied along the principal crystallographic axes by means of a home-built vibrating sample magnetometer [21] (VSM) and in fields up to 5 T in a Quantum Design MPMS-XL5 SQUID magnetometer. Pulsed-magnetic-field magnetization was studied up to 60 T at Helmholtz Zentrum Dresden Rossendorf by an induction method using a coaxial pick-up coil system [22]. The pulse raising time was 7 ms. The pulsed-field magnetization data were calibrated using static magnetic field measurements. Specific heat measurements at 0 T and 9 T has been done in a Quantum Design PPMS using a relaxation method. The relative length changes dL_i/L_i were studied on a cuboid shaped single crystal of dimensions $2 \times 1.85 \times 1$ mm^3. The measurements were done by means of a three-terminal high-resolution capacitance dilatometer [23]. In order to investigate the effect of magnetic fields, the linear thermal expansion coefficient $\alpha_i = 1/L_i dL_i(T)/dT$ was studied in magnetic fields up to 15 T. In addition, the field induced length changes $dL_i(B)/L_i$ were measured at various fixed temperatures in magnetic fields up to 15 T and the longitudinal magnetostriction coefficient $\lambda_i = 1/L_i dL_i(B)/dB$ was derived. The magnetic field was applied along the direction of the measured length changes.

III. $NiTiO_3$ SINGLE CRYSTAL GROWTH

Single crystals of $NiTiO_3$ were grown by the optical floating-zone method using polycrstalline feed and seed rods as starting material. The phase purity of the $NiTiO_3$ powders used for making the feed and seed rods has been studied by means of powder XRD after each sintering step. Rietveld refinement of these data indicates the presence of ilmenite phase (R-3) as well as an additional ($\approx 1\%$) TiO_2 (rutile) phase. In order to achieve phase pure high-quality single crystals, a variety of crystal growth experiments were performed under different atmosphere and pressure and by means of both the four-mirror horizontal configuration and two-mirror vertical configuration optical furnaces [24,25]. The optimized growth parameters employed during crystal growth are listed in Table I.

TABLE I. Growth parameters, lattice parameters, and phase analysis from the Rietveld refinement of the room temperature powder XRD data of crushed $NiTiO_3$ single crystals. Feed and seed rods were counter-rotated at the same rotation speed.

Furnace	CSC	CSC	HKZ
Atmosphere	O_2	air	Ar
Pressure	Ambient	Ambient	5 bar
Growth rate (rpm)	3	3	4-6
Rotation speed (mm/h)	20	10	15
Latt. parameter a (Å)	5.0304	5.0304	5.0304
Latt. parameter c (Å)	13.7881	13.7845	13.7862
Crystal size	cm	cm	mm
Secondary phase (appr.)	1% TiO_2 + NiO	1% TiO_2	1% NiO

Depending on the growth parameters, the processes summarized in Table I yield mm- to cm-sized single crystals. Figure 1(a) shows a representative $NiTiO_3$ boule grown in air at ambient pressure. The shiny surface of the grown boule indicating the presence of single crystal of several cm in length. Rietveld refinement of powder XRD data of the ground and pulverized single crystalline pieces extracted from the boules [see Fig. 1(b) and Table I] implies the main ilmenite

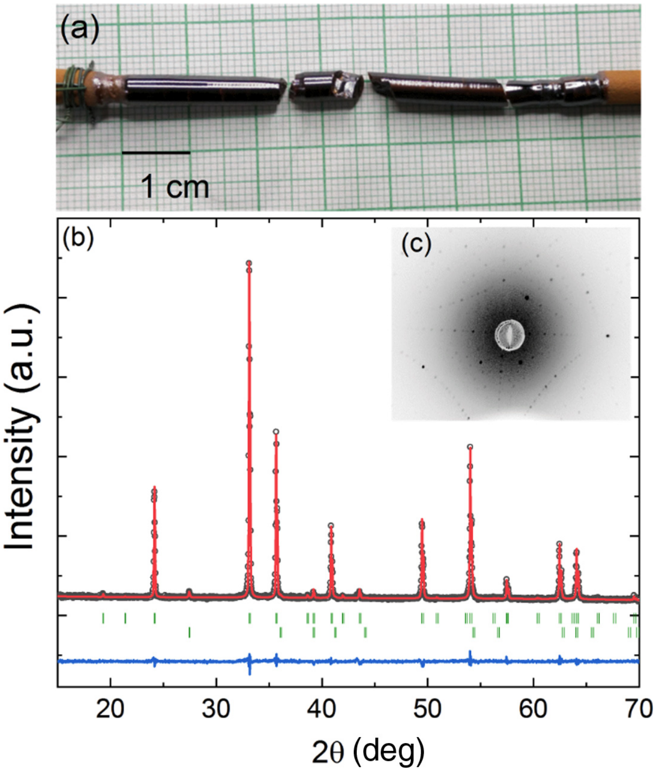

FIG. 1. (a) Picture of a shiny $NiTiO_3$ boule grown in air atmosphere at ambient pressure and (b) Rietveld refinement fit of the room temperature XRD data of a powdered $NiTiO_3$ single crystal. The observed diffraction pattern is shown in black, calculated pattern in red and the difference between the observed and the calculated pattern is shown in blue. The upper vertical ticks in green denote the allowed Bragg positions of the ilmenite phase and the lower ticks denote the Bragg positions of TiO_2 in rutile phase. (c) Representative Laue pattern of the $NiTiO_3$ single crystal oriented along (010) direction.

phase as well as an impurity TiO_2 phase of about 1%. When grown in O_2 atmosphere, there is also an additional NiO phase. In order to further investigate the growth process of $NiTiO_3$ and to reduce the secondary phase content, $NiTiO_3$ was also grown under 5 bar pressure in Ar atmosphere. In this case, the resulting boule is mostly of polycrystalline nature with only mm-sized shiny single crystalline regions toward the end of the boule. Phase analysis of a single crystalline piece extracted from this region shows the presence of about 1 % NiO secondary phase while the TiO_2 phase is absent. We conclude that inert atmosphere does not support optical floating-zone-growth of $NiTiO_3$ single crystals. For the magnetic studies presented below, we employ crystals grown in air as they exhibit only a small nonmagnetic impurity phase. Laue diffraction performed at several spots along the length of grown boules confirm the presence of macroscopic cm-sized single crystalline grains with high crystallinity [see Fig. 1(c)]. For the measurements reported below, a cuboid shaped single crystal of dimensions $2 \times 1.85 \times 1\,\mathrm{mm}^3$ has been extracted from the boule grown in air and oriented along three principal crystallographic directions.

IV. EXPERIMENTAL RESULTS

A. Magnetoelastic coupling

The onset of long-range antiferromagnetic order in $NiTiO_3$ at $T_N = 22.5(5)$ K is associated with pronounced anomalies in magnetic susceptibility and specific heat (Fig. 2). For $T \leqslant T_N$, the susceptibility is anisotropic with a decrease for magnetic fields B applied in the ab plane and attaining a constant value for $B||c$ axis suggesting an easy-plane-type antiferromagnet. This is in accordance with the previous studies [4,6]. At high temperatures, the susceptibility is isotropic and obeys a Curie-Weiss behavior. Fitting the averaged susceptibility [inset to Fig. 2(a)] at $T > 100$ K by means of a Curie-Weiss-like law $\chi = \chi_0 + N_A\mu_{\mathrm{eff}}^2/3k_B(T-\Theta)$ yields $\chi_0 = 1.93 \times 10^{-4}$, the effective magnetic moment $\mu_{\mathrm{eff}} = 3.17(5)\ \mu_B$ and the Weiss temperature $\Theta = -11(1)$ K. Using the spin-only value $S = 1$ for Ni^{2+} implies an effective g factor of 2.24(4). Note, that our measurements yield a smaller value than $\mu_{\mathrm{eff}} = 4.01\ \mu_B$ previously reported for a single crystal [4] but is similar to the values reported for polycrystalline samples [3,11].

The sharp λ-shaped anomalies in the specific heat [Fig. 2(b)] and in Fisher's specific heat [26] $\partial(\chi_a T)/\partial T$ [Fig. 2(a)] confirm the onset of long-range magnetic order at T_N and also indicate high crystallinity of the single crystal. Furthermore, the anomaly presents a continuous nature of the phase transition. The phonon contribution to the specific heat (c_p^{ph}) has been estimated by fitting the c_p data at temperatures well above T_N by an extended Debye model which includes both Debye and Einstein terms [27]. The model fits very well for temperatures above about 50 K and yields characteristic Debye and Einstein temperatures of $\Theta_D = 786$ K and $\Theta_E = 230$ K, respectively. The sum of the obtained coefficients of the individual terms $n_D = 3.94$ and $n_E = 0.94$ reasonably agrees to the expected value of 5 which reflects the number of phonon modes given by the number of atoms per formula unit. Integrating the magnetic specific heat $(c_p\text{-}c_p^{\mathrm{ph}})/T$ yields a total magnetic entropy change $S_{\mathrm{mag}} = 9.1(1)$ J/(mol K) which agrees to the theoretically expected value for $S = 1$ Ni^{2+} spins of $R\ln(3) = 9.13$ J/(mol K). We conclude that the entropy changes are of magnetic nature. The measured entropy changes imply that nearly 20% of magnetic entropy is consumed between T_N and 50 K, suggesting the presence of short-range magnetic correlation persisting up to temperatures as high as twice the ordering temperature.

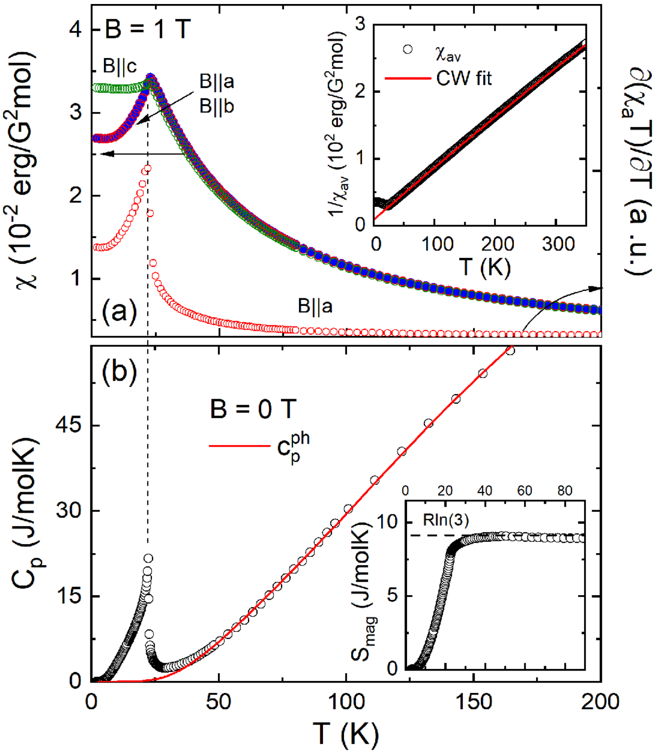

FIG. 2. (a) Temperature dependence of the static magnetic susceptibility $\chi = M/B$ (left axis) and the derivative $\partial(\chi T)/\partial T$ (right axis) at $B = 1$ T applied along main crystallographic directions and (b) temperature dependence of the specific heat c_p in zero magnetic field. The solid line in (b) indicates the phonon specific heat c_p^{ph} obtained by fitting c_p data with a combined Debye and Einstein model well above the magnetic ordering transition (see the text). Insets: (a) Curie-Weiss fit (red line) to the inverse averaged susceptibility $1/\chi_{\mathrm{av}}$. (b) Magnetic entropy changes obtained by integrating $(c_p\text{-}c_p^{\mathrm{ph}})/T$.

The evolution of long-range magnetic order is associated with pronounced length changes as illustrated by strong anomalies in the uniaxial thermal expansion coefficients α_i ($i = a, c$) and in the relative length changes dL_i/L_i (Fig. 3). The anomalies demonstrate the presence of significant magnetoelastic coupling in $NiTiO_3$. The measured relative length changes shown in the inset of Fig. 3 signal shrinking of the c axis and increase of the a axis on evolution of magnetic order at T_N. The signs of the anomalies indicate positive uniaxial pressure dependence of T_N for pressure along c axis, i.e., $\partial T_N/\partial p_c > 0$, whereas the anomaly in α_a indicates $\partial T_N/\partial p_a$ being negative and considerably smaller. The anomaly in the volume thermal expansion coefficient $\alpha_V = \alpha_c + 2\alpha_a$ implies a significant positive hydrostatic pressure dependency of T_N. In addition, opposite sign of the anomalies in α_a and α_c enables reading-off the data in Fig. 3 that structural effects

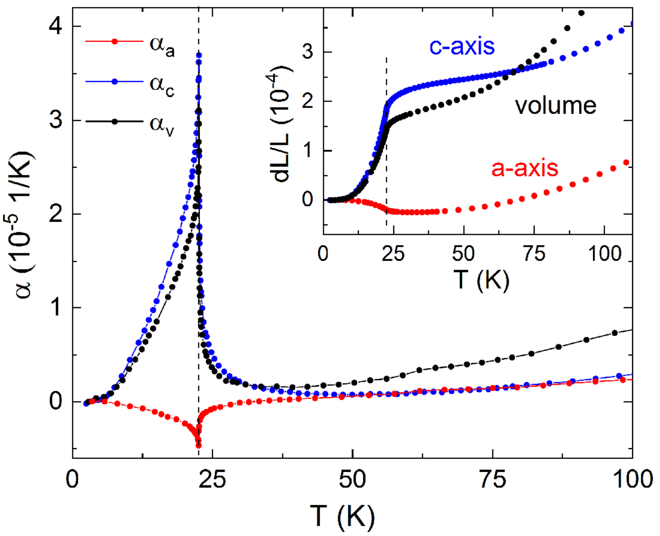

FIG. 3. Thermal expansion coefficients α_i along the crystallographic a and c axes and the volume thermal expansion coefficient α_V. The inset shows the relative length changes dL_i/L_i. Dashed lines mark T_N.

above T_N precursing the onset of long-range order extend up to about 50 K. This coincides with the temperature regime where magnetic entropy changes mark the onset of short-range magnetic correlations.

B. Magnetic phase diagram

The saturation fields and moments at $T = 1.5$ K are deduced from pulsed-field magnetization studies up to 60 T which are shown in Fig. 4(a). For both field directions $B||c$ and $B||a$, the magnetization shows a linear behavior in a wide range of applied fields. The saturation fields nearly coincide and amount to $B_{\text{sat}} = 36.0(5)$ T. Also the saturation magnetisations as indicated by the dashed horizontal lines in Fig. 4(a) agree with each other within error bars at $M_{\text{sat}} = 2.23(5)$ μ_B/f.u.. For $S = 1$, this yields $g = 2.23(5)$ which agrees well with the value of 2.24(4) derived from the Curie-Weiss fit to the static magnetic susceptibility presented in Fig. 2. A more detailed look at the low-field behavior in Fig. 4(b), at $T = 2$ K, confirms that linearity of M vs. $B||c$ extends to zero magnetic field while nonlinear behavior is observed when the magnetic field is applied along the a axis. To be specific, the derivative of the magnetization with respect to magnetic field shows a broad peak centered at $B^* = 1.20(5)$ T and subsequently a constant behavior [see Fig. 4(b)]. The data suggest spin reorientation which we attribute to finite anisotropy in the ab plane. At $T = 2$ K, the magnetization jump at B^* is estimated to $\Delta M \approx 0.03$ μ_B/f.u. Remaining slight nonlinearity above B^* is indicated by the static magnetic susceptibility measured in magnetic fields up to 15 T [Figs. 4(c) and 4(d)]. While there is no significant field effect for $T > T_N$, the data exhibit a monotonous change for $T < T_N$ at applied fields $B \geqslant 3$ T as compared to $B = 1$ T. Overall, the data confirm spin-reorientation behavior as for $B \geqslant 3$ T (i.e., above B^*) the susceptibility attains an almost constant value below T_N whereas it decreases sharply for $B||a = 1$ T.

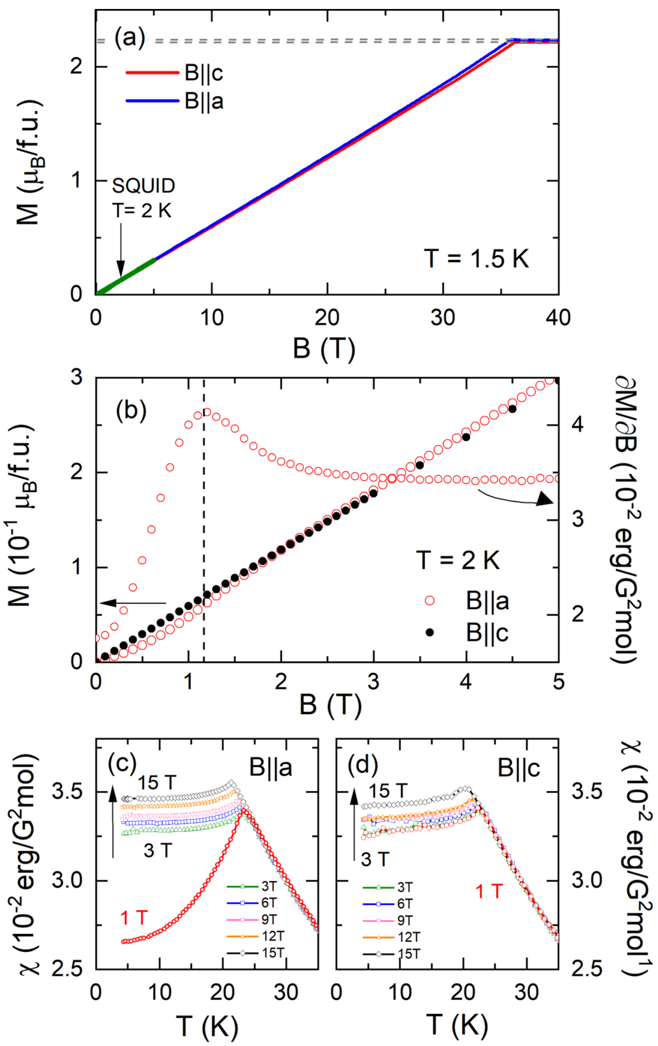

FIG. 4. (a) Pulsed-field magnetization M at $T = 1.5$ K, (b) quasistatic field magnetization M and magnetic susceptibility $\partial M/\partial B$ vs. magnetic field along the a- and c axes, at $T = 2$ K, [(c) and (d)] static magnetic susceptibility $\chi = M/B$ vs. temperature for magnetic fields up to 15 T applied along the a- and c axes, respectively.

In addition, the phase boundary T_N (B) marked as peak in the static susceptibility is determined.

Sharp λ-shaped anomalies observed in α_i ($i = a, c$) in external magnetic fields (Fig. 5) enable to further determine the phase boundaries and to study the magnetic field effect on the lattice parameters. While the shape of the anomalies are not significantly affected by magnetic fields, T_N expectedly shifts to lower temperatures on application of external magnetic fields. For both field directions, a similar shift of $\Delta T_N \approx 1.5$ K is observed when applying $B = 15$ T. This corroborates well with the magnetization data in Figs. 4(c) and 4(d) and signals overlying phase boundaries for B applied along the a and c axes, respectively (see Fig. 6). Corresponding anomalies signaling $T_N(B)$ (or synonymously the temperature dependence of the critical field $B_c(T)$ which signals melting of magnetic order, too) appear in the relative length changes versus magnetic field (Fig. 7) and in the magnetostriction coefficients (see supplemental material, Fig. S1 [34]) and

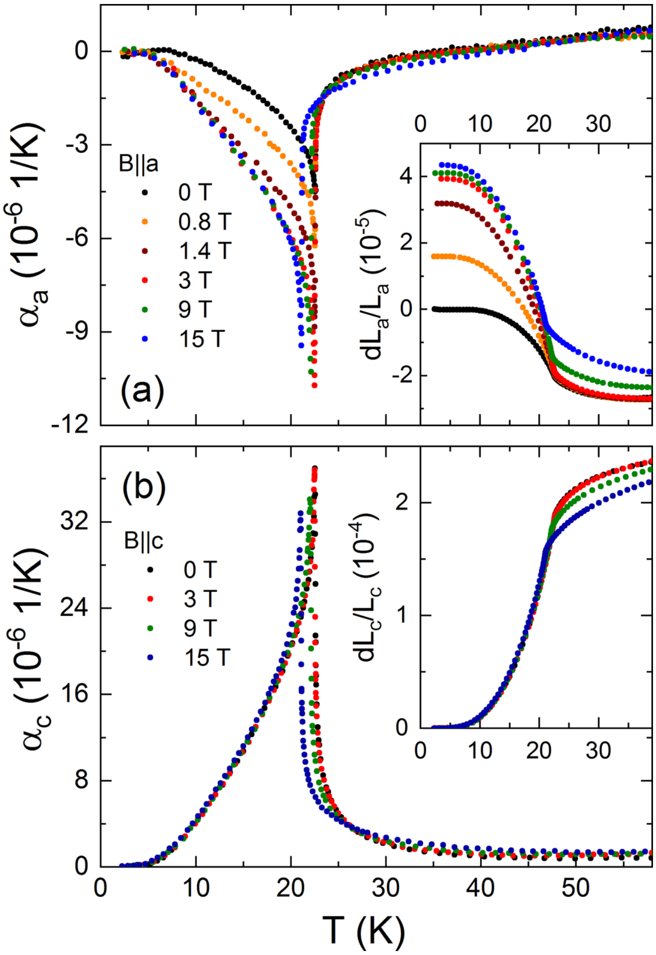

FIG. 5. Thermal expansion coefficients α_i at magnetic fields between 0 T and 15 T applied along the *a*- and *c* axes, respectively, of NiTiO$_3$. Insets show the corresponding relative length changes shifted with respect to each other by means of magnetostriction curves, at $T = 30$ K.

enable constructing the magnetic phase diagram displayed in Fig. 6. To 15 T, $T_N(B)$ obeys a square-root behavior.

The thermal expansion in magnetic field and the magnetostriction data in Figs. 5 and 7, respectively, show small increase of the *a* axis and decrease of the *c* axis in magnetic fields applied in the respective directions. Interestingly, except for effects associated with suppression of T_N, there are no large length changes dL_c driven by $B\|c \leqslant 15$ T. Correspondingly, the magnetostriction λ_c, at 2 K (see supplemental material, Fig. S1 [34]), is small and amounts to a few 10^{-7} T^{-1} only. While a similar behavior is found for λ_a at $B\|a \gtrsim 5$ T, there are pronounced length changes at low fields which we associate with spin-reorientation. The corresponding half height of these jump like anomalies in dL_a/L_a is at consistent fields as the peak in $\partial M/\partial B$ and yields B^* (see Fig. 6). Notably, these field-induced changes imply that the total thermal expansion changes in the magnetically ordered phase become considerably larger in applied magnetic fields [see the inset of Fig. 5(a)]. Quantitatively, spin reorientation at 2 K is associated with length changes of $\Delta L_a/L_a \approx 4.8 \times 10^{-5}$. On heating, the size of magnetostriction decreases but,

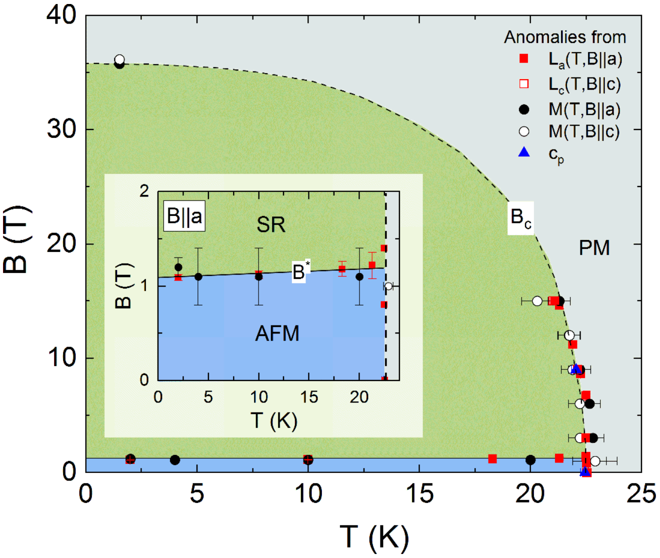

FIG. 6. Magnetic phase diagram of NiTiO$_3$ constructed from magnetization $M(T, B)$, dilatometry $L(T, B)$ and specific heat data. Closed (open) markers correspond to magnetic fields applied along the *a* axis (*c* axis). Lines are guides to the eye. AFM, SR, PM label the antiferromagnetically ordered, spin-reoriented and paramagnetic phases, respectively.

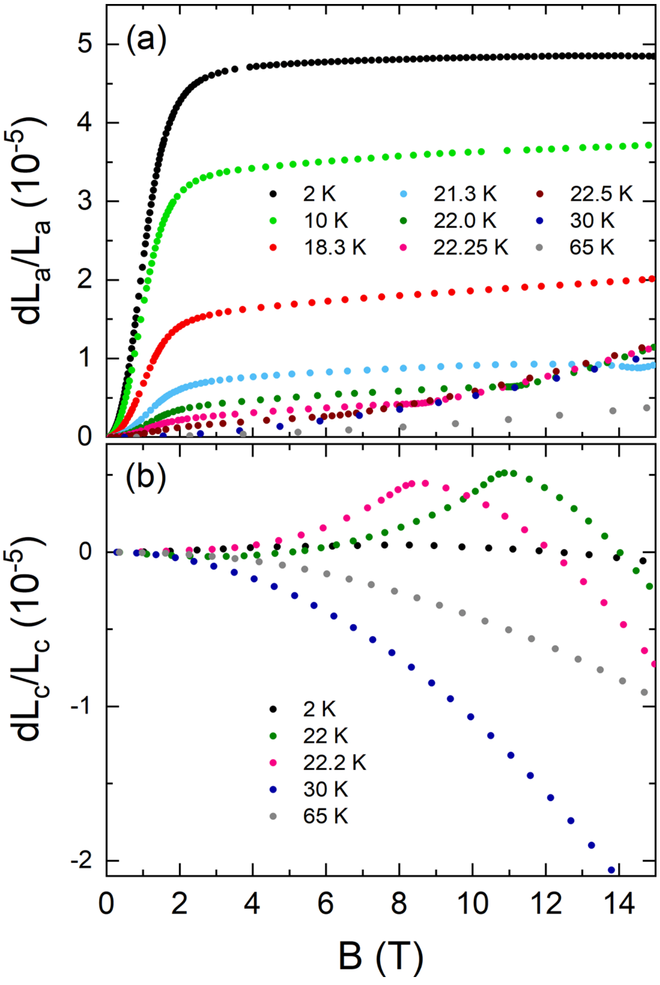

FIG. 7. Relative length changes versus magnetic field applied along *a* and *c* axes at different temperatures.

nonetheless, significantly exceeds length changes observed at $T > T_N$.

C. Discussion

Knowledge on the saturation fields $B_{\rm sat}$ enables estimating the effective antiferromagnetic exchange interaction $J_{\rm AF}$ driving the A-type nature of magnetic order. Applying a two-sublattice mean-field model, the saturation field, at $T = 0$, is determined by interplane interaction and magnetic anisotropy. The fact that $B_{\rm sat}$ does not depend on the magnetic field direction, i.e., $B_{\rm sat}^{||} \simeq B_{\rm sat}^{\perp}$, suggests a negligible effect of the latter. By employing

$$g\mu_B B_{\rm sat} = E(\uparrow\downarrow) - E(\uparrow\uparrow) = 2J_{\rm AF}$$

we obtain the effective interplanar exchange coupling $J_{\rm AF}/k_B = 25.1(5)$ K. Here $E(\uparrow\downarrow)$ denotes the energy associated with the A-type AFM state at $B = 0$ and $E(\uparrow\uparrow)$ that of the fully spin-polarized state at $B > B_{\rm sat}$. In addition, validity of the Curie-Weiss law down to nearly T_N indicates that mean-field equations relating experimental values of the Weiss temperature Θ and the Néel temperature T_N can be used to estimate effective in-plane and interplane couplings $J_{\rm FM}$ and $J_{\rm AF}$. Following Refs. [28,29], we obtain $J_{\rm AF}/k_B = 25.1(5)$ K which agrees very well with analysis of $B_{\rm sat}$, and $J_{\rm FM} = 8.5(5)$ K.

Comparing the nonphononic contributions to the thermal expansion coefficient and to the specific heat enables further conclusions on the nature of the associated (i.e., magnetic) entropy changes and on the hydrostatic pressure dependencies. In order to assess the magnetic contribution to the volume thermal expansion coefficient, $\alpha_V^{\rm mag}$, we have approximated the phonon contribution, $\alpha_V^{\rm ph}$, by scaling the background specific heat $c_p^{\rm ph}$ (cf. Fig. 2) by means of an appropriate Grüneisen parameter $\gamma^{\rm ph} = \alpha_V^{\rm ph}/c_p^{\rm ph}$ [30]. For that purpose, a Debye-Einstein model with fixed Θ_D and Θ_E of the fit to the specific heat data has been fitted to the high-temperature data of α_V leaving only the two associated lattice Grüneisen parameters γ_D and γ_E as scaling factors. Similarly to the specific heat, at $T \gtrsim 50$ K, α_V is well described by the phonon background $\alpha_V^{\rm ph}$ with $\gamma_D = 2.8 \times 10^{-7}$ mol/J and $\gamma_E = 2.3 \times 10^{-7}$ mol/J as shown in the inset of Fig. 8.

The resulting nonphonon contribution $\alpha_V^{\rm mag}$ to the thermal expansion coefficient is shown in Fig. 8(a) (right ordinate) together with the respective magnetic specific heat data $c_p^{\rm mag}$ (left ordinate). Both quantities are proportional to each other in the entire temperature range, i.e., there is a T-independent Grüneisen parameter describing the ratio of pressure and temperature dependence of entropy changes in this temperature range. This observation clearly implies the presence of a single dominant energy scale ϵ [31]. As entropy changes are of magnetic nature, we conclude that a single magnetic degree of freedom drives the observed nonphonon length and entropy changes. The corresponding scaling parameter obtained is the magnetic Grüneisen parameter [30]

$$\gamma_m = \frac{\alpha_V^{\rm mag}}{c_p^{\rm mag}} = \frac{1}{V}\frac{\partial \ln \epsilon}{dp}\bigg|_T = 1.18(3) \times 10^{-6}\text{mol/J}.$$

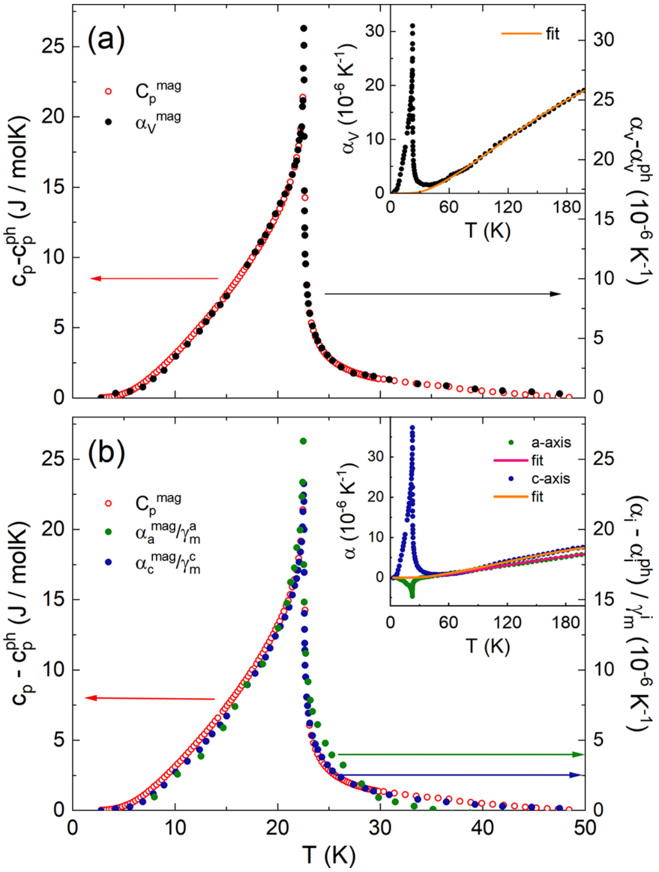

FIG. 8. Grüneisen scaling of the magnetic contributions to the heat capacity ($c_p^{\rm mag}$) and (a) volume thermal expansion coefficient ($\alpha_V^{\rm mag}$). The inset shows α_V vs. temperature together with a combined Debye-Einstein fit to the high-temperature data (see the text). (b) Grüneisen scaling with uniaxial thermal expansion coefficients α_a and α_c.

Using the Ehrenfest relation, the obtained value of γ_m enables to determine the hydrostatic pressure dependence of the ordering temperature, i.e., $dT_N/dp = T_N V_m \gamma_m = 1.12(4)$ K/GPa which is deduced using the molar volume of $V_m = 42.01$ cm^3/mol. Elaborating Grüneisen scaling for the uniaxial thermal expansion coefficients individually, good proportionality is confirmed between $c_p^{\rm mag}$ and $\alpha_a^{\rm mag}$ and $\alpha_c^{\rm mag}$ as well [Fig. 8(b)]. This yields the uniaxial pressure dependencies of $dT_N/dp_a = -0.21(3)$ K/GPa and $dT_N/dp_c = 1.51(7)$ K/GPa for pressure applied along the a and c axis, respectively. The uniaxial values are fully consistent with the obtained hydrostatic pressure dependence.

On a microscopic level (see supplemental material, Fig. S4 [34]), Ni-O-Ni bonding angles in the ab planes of 90.5(3)° implying nearest-neighbor FM exchange interaction J_{nn} are supposed to increase when hydrostatic pressure is applied, i.e., J_{nn} becomes smaller. The main exchange paths contributing to $J_{\rm AF}$ do not suggest a clear picture which prohibits a qualitative analysis.

Magnetostriction measurements in the paramagnetic regime, i.e., where $M = \chi B$, enable to extract the uniaxial pressure dependence of magnetic susceptibility by exploiting the relation $dL_i/L_i = -1/2V\partial\chi_i/\partial p_i B^2$ [32].

Plotting the data accordingly (see supplemental material Fig. S2 [34]) allows to read off $\partial(\ln\chi_a)/\partial p_a = -1.3\%\,\mathrm{GPa}^{-1}$ and $-0.8\%\,\mathrm{GPa}^{-1}$ at 30 and 65 K, respectively, as well as $\partial(\ln\chi_c)/\partial p_c = +3.1\%\,\mathrm{GPa}^{-1}$ and $+2.2\%\,\mathrm{GPa}^{-1}$ at respective temperatures. Qualitatively, this suggests AFM exchange interactions to be strengthened and FM ones to be weakened by uniaxial pressure along the a axis. While, uniaxial pressure along the c axis is found to result in opposite effects. Considering the results of Grüneisen analysis presented above, i.e., predominance of only one energy scale as well as $\partial T_N/\partial p_a < 0$ and $\partial T_N/\partial p_c > 0$, suggests that the value of T_N is mostly affected by the (in-plane) FM exchange interactions. This is also reflected in the increase of T_N and Weiss temperature θ when substituting Ni over Co to Fe in $M\mathrm{TiO}_3$ whereby even $\theta > 0$ is observed for FeTiO_3 [3].

The phase boundary of spin-reorientation features a very small slope $\partial B^*/\partial T \approx 4 \times 10^{-3}$ T/K. Considering the magnetization jump ΔM at B^* and exploiting the Clausius-Clapeyron relation, we estimate associated entropy changes $\Delta S^* = -(\partial T/\partial B^*)^{-1} \cdot \Delta M^* \approx -8 \times 10^{-4}\,\mathrm{J/(mol\,K)}$ [33]. This implies only insignificant entropy changes associated with spin reorientation. On the other hand, in applied magnetic fields $B\|a$, our data show that the total thermal expansion changes dL_a/L_a in the magnetically ordered phase become significantly larger (see the inset of Fig. 5). This suggests that Grüneisen scaling which is valid at $B = 0\,\mathrm{T}$ as evidenced by Fig. 8 is broken in magnetic fields $B||a > B^*$. Somehow correspondingly, uniaxial pressure dependence of B^* is very large. Using the measured jumps in relative length changes $(\Delta L_a/L_a)$ and magnetization (ΔM) at B^* and 2 K and exploiting the Clausius-Clapeyron relation yields $\partial B^*/\partial p_a = V(\Delta L_a/L_a)/\Delta M \approx 9.2\,\mathrm{T/GPa}$. This is a huge value similar to what has been observed, i.e., in TlCuCl_3 [32]. It implies strong effects of uniaxial pressure along the a axis so that applying p_a would strongly enhance the spin reorientation field while it would vanish for tiny hypothetical negative pressure.

Below T_N, due to the presence of small in-plane anisotropy one might assume that magnetostriction would locally distort the lattice to a lower symmetry $P-1$. While such symmetry breaking has not yet been observed in previous neutron diffraction experiments, the fact that this distortion is expected to increase with application of magnetic field might allow detecting such symmetry breaking when applying external magnetic fields. Above T_N, i.e., in the absence of long-range spin order where short-range correlations are still present as, e.g., indicated by the specific heat data, magnetostriction is relatively large in NiTiO_3. This observation agrees to the fact that both λ_a and λ_c become significantly larger when B exceeds B_c which appears at 21 K $\leqslant T \leqslant$ 22.2 K in the accessible field range (see Fig. 7 and supplemental material, Fig. S1 [34]). We conclude that, in a paramagnetic but yet correlated regime, magnetic fields along the a and the c axes, respectively, yield reorientation of spins which are short-range ordered in this temperature and field ranges.

Recently, anomalies in the electrical permittivity ϵ at T_N and strongly field-dependent magnetocapacitance close to T_N have been observed in polycrystalline NiTiO_3 indicating the presence of significant magnetodielectric coupling [11]. The shape of the reported temperature dependence of ϵ is very similar to the length and volume changes observed by our thermal expansion measurements (see supplemental material Fig. S3 [34]) indicating an almost linear relation between electrical permittivity and structural distortion below T_N. Conclusively, $\epsilon(T)$ and reported magnetodielectric coupling are directly related to the length changes and the magnetoelastic coupling. Furthermore, driving entropy changes of the low-temperature effects are purely of magnetic nature as evidenced by Grüneisen analysis presented above. We conclude that magnetodielectric coupling is secondarily mediated via structural changes and that magnetic degrees of freedom constitute a single common origin for the dielectric, structural and magnetic changes evolving at and below T_N in NiTiO_3. Note, however, that magnetocapacitance data on polycrystals (at $T = 15\,\mathrm{K}$) do not show anomalies at B^* though spin reorientation is associated with significant length changes. One might speculate that the polycrystalline nature of samples studied in Ref. [11] masks such effects.

V. SUMMARY

In summary, we report growth and characterization of large and high quality NiTiO_3 single crystals by means of the optical floating-zone technique. The anisotropic phase diagram is constructed by means of pulsed and static magnetization, specific heat, thermal expansion, and magnetostriction data. It features a spin-reorientation transition at $B^*||a \approx 1.2\,\mathrm{T}$ which is accompanied by pronounced length changes. In addition, high-resolution thermal expansion data are used for detailed analysis of pronounced magnetoelastic coupling in NiTiO_3. Grüneisen scaling of the magnetic contributions to c_p and α_V implies a single magnetic degree of freedom driving the observed length and entropy changes at T_N. Our analysis suggests in-plane ferromagnetic interactions mainly determine the value of T_N. Relating our findings to recently reported strong magnetodielectric effects in NiTiO_3 implies the essential role of structural changes for magnetodielectric coupling and suggests a single magnetic origin of low-temperature dielectric, structural, and magnetic changes in NiTiO_3.

ACKNOWLEDGMENTS

Funding by the Federal Ministry of Education and Research (BMBF) under contract 13XP5088 SPINFUN is gratefully acknowledged. S.S., J.W., and R.K. acknowledge support by Deutsche Forschungsgemeinschaft through project KL1824/13-1. K.D. acknowledges fellowship by the IMPRS-QD. S.S. acknowledges financial support from the Science and Engineering Research Board (SERB) under Grant No. EMR/2016/003792. We acknowledge the support of the HLD at HZDR, member of the European Magnetic Field Laboratory.

---

[1] N. A. Spaldin and M. Fiebig, Science **309**, 391 (2005).
[2] T. F. W. Barth and E. Posnjak, Z. Krist. **88**, 265 (1934).
[3] J. J. Stickler, S. Kern, A. Wold, and G. S. Heller, Phys. Rev. **164**, 765 (1967).

[4] H. Watanabe, H. Yamauchi, and H. Takei, J.Magn. Magnetic Mat. **15-18**, 549 (1980).
[5] G. S. Heller, J. J. Stickler, S. Kern, and A. Wold, J. Appl. Phys. **34**, 1033 (1963).
[6] G. Shirane, S. J. Pickart, and Y. Ishikawa, J. Phys. Soc. Jpn. **14**, 1352 (1959).
[7] R. E. Newnham, J. H. Fang, and R. P. Santoro, Acta Crystallogr. **17**, 240 (1964).
[8] Y. Yamaguchi, H. Kato, H. Takei, A. Goldman, and G. Shirane, Solid State Commun. **59**, 865 (1986).
[9] M. Charilaou, D. Sheptyakov, J. F. Löffler, and A. U. Gehring, Phys. Rev. B **86**, 024439 (2012).
[10] N. Mufti, G. R. Blake, M. Mostovoy, S. Riyadi, A. A. Nugroho, and T. T. M. Palstra, Phys. Rev. B **83**, 104416 (2011).
[11] J. K. Harada, L. Balhorn, J. Hazi, M. C. Kemei, and R. Seshadri, Phys. Rev. B **93**, 104404 (2016).
[12] B. Yuan, I. Khait, G.-J. Shu, F. C. Chou, M. B. Stone, J. P. Clancy, A. Paramekanti, and Y.-J. Kim, Phys. Rev. X **10**, 011062 (2020).
[13] C. dela Cruz, F. Yen, B. Lorenz, Y. Q. Wang, Y. Y. Sun, M. M. Gospodinov, and C. W. Chu, Phys. Rev. B **71**, 060407(R) (2005).
[14] C. R. de la Cruz, B. Lorenz, Y. Y. Sun, C. W. Chu, S. Park, and S. W. Cheong, Phys. Rev. B **74**, 180402(R) (2006).
[15] M. Ackermann, L. Andersen, T. Lorenz, L. Bohatý, and P. Becker, New J. Phys. **17**, 013045 (2015).
[16] L. Wang, J. Werner, A. Ottmann, R. Weis, M. Abdel-Hafiez, J. Sannigrahi, S. Majumdar, C. Koo, and R. Klingeler, New J. Phys. **20**, 063045 (2018).
[17] Y. Zhang, M. McDonnell, S. A. Calder, and M. G. Tucker, J. Am. Chem. Soc. **141**, 6310 (2019).
[18] C. P. Grams, S. Kopatz, D. Brüning, S. Biesenkamp, P. Becker, L. Bohatý, T. Lorenz, and J. Hemberger, Sci. Rep. **9**, 4391 (2019).
[19] N. Awadhesh, A. Cano, A. V. Balatsky, and N. A. Spaldin, Nat. Mat. **18**, 223 (2019).
[20] J. Rodríguez-Carvajal, Physica B: Condens. Matt. **192**, 55 (1993).
[21] R. Klingeler, B. Büchner, K.-Y. Choi, V. Kataev, U. Ammerahl, A. Revcolevschi, and J. Schnack, Phys. Rev. B **73**, 014426 (2006).
[22] Y. Skourski, M. D. Kuz'min, K. P. Skokov, A. V. Andreev, and J. Wosnitza, Phys. Rev. B **83**, 214420 (2011).
[23] R. Küchler, T. Bauer, M. Brando, and F. Steglich, Rev. Sci. Inst. **83**, 095102 (2012).
[24] W. Hergett, C. Neef, H. Wadepohl, H.-P. Meyer, M. M. Abdel-Hafiez, C. Ritter, E. Thauer, and R. Klingeler, J.Cryst. Growth **515**, 37 (2019).
[25] C. Neef, H. Wadepohl, H.-P. Meyer, and R. Klingeler, J. Cryst. Growth **462**, 50 (2017).
[26] M. E. Fisher, Philos. Mag. **7**, 1731 (1962).
[27] N. Aschcroft and N. Mermin, *Solid State Physics* (Saunders College, Philadelphia, 1976).
[28] J. B. Goodenough and J. J. Stickler, Phys. Rev. **164**, 768 (1967).
[29] W. Nolting and A. Ramakanth, *Quantum Theory of Magnetism* (Springer, Berlin, 2009).
[30] R. Klingeler, J. Geck, S. Arumugam, N. Tristan, P. Reutler, B. Büchner, L. Pinsard-Gaudart, and A. Revcolevschi, Phys. Rev. B **73**, 214432 (2006).
[31] P. Gegenwart, Rep. Prog. Phys. **79**, 114502 (2016).
[32] N. Johannsen, A. Vasiliev, A. Oosawa, H. Tanaka, and T. Lorenz, Phys. Rev. Lett. **95**, 017205 (2005).
[33] U. Stockert, N. Leps, L. Wang, G. Behr, S. Wurmehl, B. Büchner, and R. Klingeler, Phys. Rev. B **86**, 144407 (2012).
[34] See supplemental material at http://link.aps.org/supplemental/10.1103/PhysRevB.101.195122 for additional magnetostriction data, the comparison of the thermal expansion coefficient and the normalized dielectric permittivity, and a schematic of dominant exchange pathways in $NiTiO_3$.